

Full paper

Direct-printed nanoscale metal-oxide-wire electronics

Tae-Sik Kim^{a,1}, Yeongjun Lee^{b,c,1}, Wentao Xu^{b,d,e,1}, Yeon Hoo Kim^{b,d,1}, Miseong Kim^a,
Sung-Yong Min^a, Tae Hoon Kim^{b,d}, Ho Won Jang^{b,d,*}, Tae-Woo Lee^{b,c,d,f,*}

^a Department of Materials Science and Engineering, Pohang University of Science and Technology (POSTECH), Pohang 37673, Republic of Korea

^b Department of Materials Science and Engineering, Seoul National University, Seoul 08826, Republic of Korea

^c BK21 PLUS SNU Materials Division for Educating Creative Global Leaders, Seoul National University, Seoul 08826, Republic of Korea

^d Research Institute of Advanced Materials, Seoul National University, Seoul 08826, Republic of Korea

^e Institute of Photoelectronic Thin Film Devices and Technology of Nankai University, Tianjin 300071, PR China

^f Institute of Engineering Research, Nano Systems Institute (NSI), Seoul National University, Seoul 08826, Republic of Korea



ARTICLE INFO

Keywords:

Nanowire electronics
Metal oxide nanowires
Metal oxide transistors
Nanowire printing
Synaptic transistors
Metal oxide gas sensors

ABSTRACT

One-dimensional metal oxide (MO) micro-wires and nano-wires (MOWs) can be excellent functional units for integrated and transparent electronics. However, MOWs produced using conventional synthesis methods are short, uncontrollable, and randomly-distributed, so they cannot be easily used to fabricate high-density transistor arrays with precisely-controlled MOW-channels. Here, we describe a large-scale direct-printed universal nanoscale MOW electronics which includes highly-aligned, digitally-controlled and arbitrarily-long MOW arrays and various nanoscale applications of MOW field-effect transistors (FETs), neuromorphic synaptic transistors, and gas sensors. Broad classes of pristine, doped and alloyed MOWs are fabricated, so we demonstrated all-MOWFETs composed of conducting indium oxide (In_2O_3) wires and semiconducting indium zinc oxide (IZO) wires; the devices show a high carrier mobility $\mu \sim 17.67 \text{ cm}^2 \text{ V}^{-1} \text{ s}^{-1}$, comparable to μ of MO thin-film FETs. MOW synaptic transistors show presynaptic signals dependent postsynaptic behaviors similar to biological synaptic responses; which can be promising nano-electronic units of high-density neuromorphic devices. We also demonstrated MOW gas sensors which show high response to NO_2 gas. Our direct-printed, large-scale, and individually-controlled MOW electronics would be a promising approach in development of industrially-viable MOW electronics and open new horizons for precisely-controlled inorganic MOW electronics and nanoscale printed electronics.

1. Introduction

Metal oxide (MO) semiconductors have unique material-design-concepts, efficient charge transport and optoelectronic properties, surface functionality, and high optical transparency [1–3]. Therefore, they are regarded as important alternatives to conventional silicon materials in electronics. MO micro- and nano-wires (MOWs) are emerging electronic components for transistors [4,5], memory [6,7] and sensors [8,9]. Effective methods to produce MOWs have been developed, but their chemically synthesized or grown short MOWs cannot be aligned individually and precisely between electrode pairs on large-area substrate, so they are not easily applicable to high-throughput practical MOW device arrays, e.g., transistor arrays with the identical dimension of MOW-channels (the channel width and length are defined by the number and alignment angle of MOWs between source/drain

electrodes, respectively). To overcome the limitation, it is necessary to achieve individual production of arbitrarily-long MOWs with precise position and alignment in large area. Development of a sophisticated platform that produces one-dimensional (1D) MO microstructures and nanostructures would enable efficient and inexpensive construction of integrated MO device arrays, especially when the process combines state-of-art printing technologies with use of solution processibility [10–18].

Electrohydrodynamic nanowire (e-NW) printing is a direct-printing method for fabricating continuous nanowire array on demand; it is possible to uniformly print highly-aligned nanowires of various materials on a large area and easily control the line width, number, direction, and interval of the nanowires, thereby making it possible to manufacture various electronic devices that can be industrially applicable [19–23].

* Corresponding authors at: Department of Materials Science and Engineering, Seoul National University, Seoul 08826, Republic of Korea.

E-mail addresses: twlees@snu.ac.kr (T.-W. Lee), hwjang@snu.ac.kr (H.W. Jang).

¹ These authors contributed equally to this work.

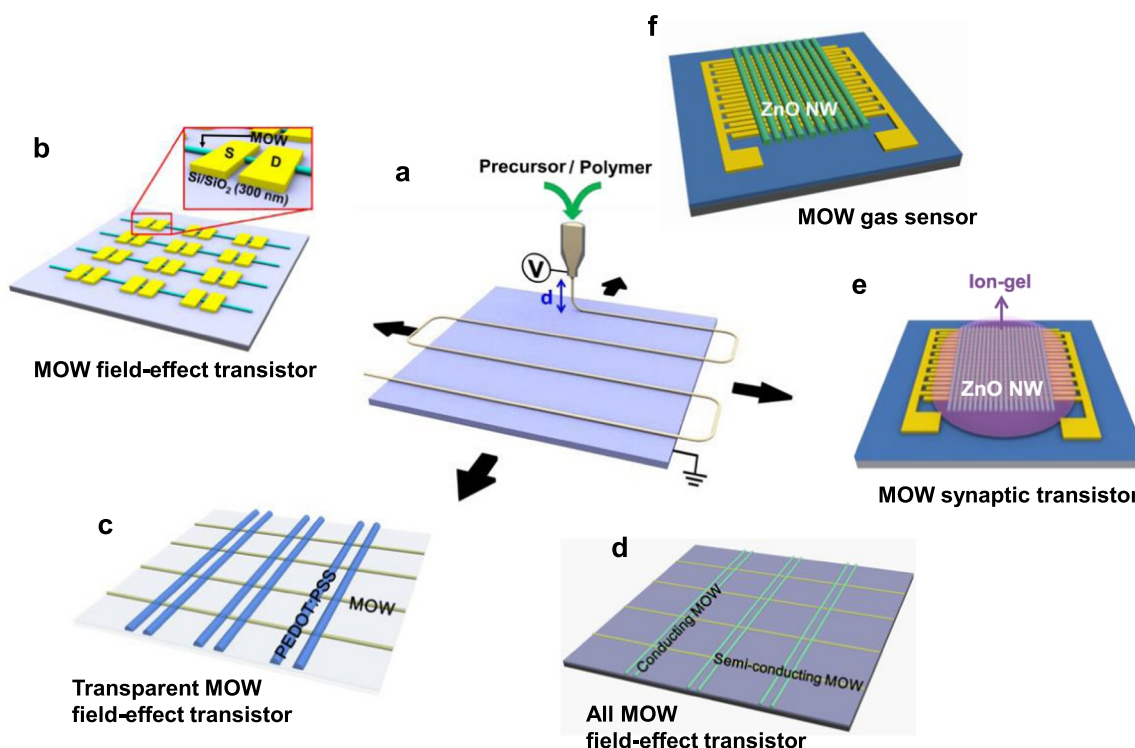


Fig. 1. Schematic of the direct-printed nanoscale MOW electronics. (a) Digitally-controlled printing of highly-aligned and arbitrarily-long wires composed of MO precursor and polymer; the precursor/polymer wires are converted to MOWs after high temperature calcination. Fabrication of (b) MOW field-effect transistors, (c) transparent MOW field-effect transistors, (d) all-MOW field-effect transistors, (e) MOW synaptic transistors, and (f) MOW gas sensors.

In this regards, we demonstrated a large-scale, highly-aligned, precisely digitally-controlled and arbitrarily-long MOW arrays and their universal applications to direct-printed nanoscale MOWs electronics such as field-effect transistors (FETs), neuromorphic artificial synapses, and gas sensors (Fig. 1). Several series of MOWFETs based on pristine, nanoparticle (NP)-doped, or alloy MOWs were fabricated; doping and alloying yielded significant improvement in electrical characteristics. All-wire transistors based on semiconducting indium zinc oxide (IZO) nanowires (NWs) and conducting indium oxide (In_2O_3) NWs were fabricated, and attained high field-effect mobility $\mu \sim 17.67 \text{ cm}^2 \text{ V}^{-1} \text{ s}^{-1}$, comparable with those of thin-film FETs. MOW-based fully-transparent FETs and neuromorphic artificial synaptic transistors were also demonstrated. As a benefit of the nanoscale structure, MOW gas sensors showed high response to NO_2 gas. These results demonstrate the potential of our unique direct-printed nanoscale MOW electronics for future industrially-viable MOW electronics.

2. Experimental section

2.1. MOW production

Poly(vinylpyrrolidone) (PVP, $M_w = 1300,000 \text{ g mol}^{-1}$) was used as a sacrificial polymer; zinc acetate dihydrate ($\text{Zn}(\text{CH}_3\text{COO})_2 \cdot 2\text{H}_2\text{O}$, ZnACD), indium nitrate hydrate ($\text{In}(\text{NO}_3)_3 \cdot x\text{H}_2\text{O}$, InNH), tin chloride dihydrate ($\text{SnCl}_2 \cdot 2\text{H}_2\text{O}$) and tungsten hexachloride (WCl_6) (all purchased from Sigma-Aldrich) were used as metallic precursors. The sacrificial polymer (15 wt%) and the metallic precursors (1:2 w-w) were dissolved in a solvent mixture (2:1 w-w) of *N,N*-Dimethylformamide (common solvent) and Tetrahydrofuran (for In_2O_3) or Ethanol (for tin oxide SnO_2 and tungsten oxide WO_3) or Trichloroethylene (for zinc oxide ZnO). Controllably-aligned blended NWs made of a sacrificial polymer and precursors were printed using our homebuilt e-NW printer according to the following steps. A solution of polymers and precursors in a gas-tight syringe was injected downward through a nozzle tip

(metallic, inner diameter $\sim 100 \mu\text{m}$). A high voltage $\sim 0.5 \text{ kV}$ was applied to the nozzle tip, while keeping a nozzle tip-to-target substrate distance of 5.5 mm. The collector that is in contact with the target substrate was grounded. The injection rate of the solution was adjusted to 170 nl min^{-1} . The fast movement of the substrate was adapted to the printing speed of the blended wires and the digitally-designed movement of the collector allows production of MOWs with neat alignment and controllable pitches. The e-NW printer digitally controls i) the solution feeding rate, ii) the magnitude of applied voltage, iii) the xyz coordinates of a printing nozzle, and iv) the movement of a high-speed robotic stage on x-y plane (moving distance, moving direction, moving speed, and moving pattern); all these parameters are critical for fabrication of NWs. The blended NWs were then converted to highly-aligned MOWs by sintering at sufficiently high temperatures in ambient air for 1 h.

2.2. Device fabrication

On a pre-cleaned 300-nm SiO_2 -coated highly-doped silicon wafer (capacitance: 11.5 nF/cm^2), the blended NWs were printed and thermally baked at sufficiently high temperature in ambient air to convert them to MOWs. Ag or Au top electrodes (100 nm thick) were deposited through a shadow mask onto MOWs by thermal evaporation. For electrolyte-gated transistors, a well-mixed ion-gel solution composed of 1-Ethyl-3-methylimidazolium bis(trifluoromethylsulfonyl)imide [EMIM][TFSI] and poly(styrene-*b*-methylmethacrylate-*b*-styrene) (PS-PMMA-PS) triblock copolymer dissolved in ethyl acetate (9.3:0.7:90, w-w: w) was dropcast on the channel region and vacuum-dried overnight to evaporate solvent.

2.3. Characterization

A Keithley 4200 semiconductor analyzer was used to obtain all electrical transport properties of field-effect transistors at room

temperature in a N₂-filled glove box. A Keysight B1500 semiconductor analyzer was used to measure electrical properties of synaptic transistors at room temperature in ambient air. The micro- and nanostructures of MOWs were investigated using X-ray diffraction (XRD, Rigaku D/MAX-2500/PC), scanning electron microscope (SEM, JEOL JSM-7401F), and transmission electron microscope (TEM, 2200FS with image Cs-corrector). X-ray photoelectron spectroscopy (XPS, AXIS Ultra DLD-Kratos, Inc) was performed using a monochromatic Al K α radiation source.

2.4. XRD measurement

The crystalline and structural properties of the MOWs were characterized by thin-film mode X-ray diffraction (Rigaku D/MAX-2500/PC) with a Cu source (Fig. S1). All the peaks can be indexed to hexagonal wurtzite ZnO (Fig. S1a). This result agrees well with JCPDS card No. 80–0075 for pure ZnO, and again confirms the formation of a pure ZnO phase after calcination above certain temperature. In XRD patterns of SnO₂, all the peaks can be indexed to tetragonal rutile structure SnO₂, thereby confirming the formation of a pure SnO₂ phase after calcination above sufficiently high temperature (Fig. S1b). In XRD patterns of the In₂O₃ nanowires, all the peaks can be indexed to the body-centered cubic structure In₂O₃ (Fig. S1c). This result agrees well with JCPDS card No. 06–0416 for pure In₂O₃, and again confirms the formation of a pure In₂O₃ phase after calcination above sufficiently high temperature. In XRD patterns of the WO₃ nanowires, all peaks can be indexed to monoclinic crystal structure WO₃; this result agrees well with JCPDS card No. 83–0951 for pure WO₃, and again confirms the formation of a pure WO₃ phase after calcination above sufficiently high temperature (Fig. S1d). The MOWs calcined at 200 °C show very weak peaks, because the organic constituents of PVP were not removed completely, and the precursors were not converted to crystal metal oxides. Definitions of the diffraction peaks improved when the samples were calcined at 500 °C. Calcination at 600 or 700 °C yielded clear and strong diffraction patterns.

2.5. Sensor measurements

As the flow gas with a constant flow rate of 1000 sccm was changed from dry air to a calibrated test gas (balanced with dry air), the variation in sensor resistance was monitored using a source measurement unit (Keithley 2365B). The sensor resistance was measured under a DC bias voltage of 1 V. The response of the sensors (R_g/R_a) was accurately determined by measuring the baseline resistances of the sensors in dry air and the fully saturated resistances after exposure to the test gas. The gas flow was controlled using mass flow controllers, and all measurements were recorded to a computer with a GPIB interface.

3. Results and discussion

3.1. MOWs array printing

Our home-built e-NW printer prints a blended solution of a sacrificial polymers and metallic precursors into arbitrarily-long and continuous solid-state wires with computer-digital control over position and alignment [19]. Solidified wires are formed at optimal nozzle-to-collector distance, voltage supply, and solution injection rate, and aligned on a collector that moves laterally according to digitally-set directions and speeds. Polymer components are then removed by high temperature calcination to leave the desired MOWs [20].

Broad classes of MO materials were used to produce various MOWs (ZnO, SnO₂, In₂O₃, WO₃) (Fig. 2a–d). Poly(vinylpyrrolidone) (PVP) were used as binding polymers. Diverse patterns were produced by digital control over the lateral moving directions and speed of the collector (Fig. 2e–h). The width of the MOWs can be controlled by adjusting printing parameters, e.g., solution concentrations (Fig. S2 and

S3), and MOWs with diameters < 100 nm can be achieved (Fig. S4). The spacing between MOWs can be controlled with resolution < 30 μ m by the robotic linear-motor stage in our printing system, but it can be further reduced by using a higher-resolution robotic motor. In detail, our e-NW printer equips a robotic stage with step movement resolution of 3 μ m, but achievement of such a high resolution is hindered by i) vibration of the robotic stage, ii) electrostatic repulsive force of charged NWs, and iii) instability of liquid jet because of dynamic air flow. Further improvement of e-NW printer and printing environment would overcome these limitations above. Average resistance and standard deviation of ZnO, In₂O₃, SnO₂ and WO₃ wires were evaluated (Fig. S5). Uniform and continuous precursor/polymer NWs were formed, and had smooth-surfaced quasi- or semi-circular cross-sections (Fig. 2a–d). The NWs arrive continuously on the substrate as solidified-state by rapid evaporation of solvent during transit after being ejected, and wires can be printed at high speed (~ 1 m s^{−1}). This technique is different from drop-on-demand (DOD) e-jet printing, which prints discrete liquid droplets to convert into continuous microscale-wide MO lines [24–26]. During DOD e-jet printing, the liquid drops collapse upon arrival at a substrate, so this method has lower resolution than our platform, and limited morphology control of the patterned line. In DOD e-jet printing, the patterned line shape is more similar to a two-dimensional flat film than to a 1D circular wires.

3.2. Morphology analysis

Calcination to remove polymeric components converted the polymer/precursor wires to MOWs: the blended wires were annealed at various calcination temperatures T_C to observe the relationship between T_C and material properties, and were converted to MOWs that consisted of nanoscale grains (Fig. S1 and S6). MOW mats of ZnO, SnO₂, In₂O₃, and WO₃ calcined for 1 h in ambient air at constant temperatures $200 \leq T_C \leq 700$ °C; X-ray diffraction (XRD) patterns revealed the formation of hexagonal wurtzite-structured ZnO [27], tetragonal rutile-structured SnO₂ [28], body-centered cubic-structured In₂O₃ [29], and monoclinic-crystal-structured WO₃ [27] after full conversion at sufficiently high T_C (Fig. S1). Grain structures were further studied in transmission electron microscopy (TEM) images of ZnO and In₂O₃ NWs (Fig. S6). ZnO NWs consisted of nanogranular grains of 5–15 nm (Fig. S6a,b); the lattice distance of 2.6 Å corresponds to the (002) plane of a wurtzite structure. Selected area electron diffraction (SAED) patterns obtained by fast Fourier transform (FFT) of the lattice image confirmed the formation of wurtzite structure (Fig. S6c). TEM images of an In₂O₃ NW show 10–15 nm nanocrystallites (Fig. S6d,e); their SAED patterns are indexed to the body-centered cubic structure (Fig. S6f).

IZO wires were also fabricated to obtain enhanced electrical characteristics in the electronic devices. Crystallinity of IZO wire can be also confirmed by high-resolution TEM (HR-TEM) (Fig. 2i–k), which shows the ZnO and In₂O₃ nanometer crystalline phases. The polycrystalline phase of the IZO wire is observed in the HR-TEM images and diffraction patterns (Fig. 2j,k) [30,31]. Energy dispersive spectroscopy (EDS) mapping of the IZO wire demonstrated that In, Zn and O, were distributed evenly in it (Fig. 2i).

In an MOW, closely-packed longitudinal nanodomains along the wire (Fig. S7) form during the multi-directional shrinkage during calcination, and are expected to increase charge carrier transport along the MOW. The multi-direction shrinkage is probably a result of differences among thermal conductivities of substrate (SiO₂, 1.38 W m^{−1} K^{−1}), air (0.0263 W m^{−1} K^{−1}) and blend of precursor (ZnO, 21 W m^{−1} K^{−1}) and polymer (high-density polymer 0.33 W m^{−1} K^{−1}) [32]. The MOWs collapsed vertically and therefore became hillock-shaped after calcination, with a width similar to that of the precursor/polymer blended wires. The precursor domains as separated by the polymer binders convert to longitudinal domains of MO during calcination.

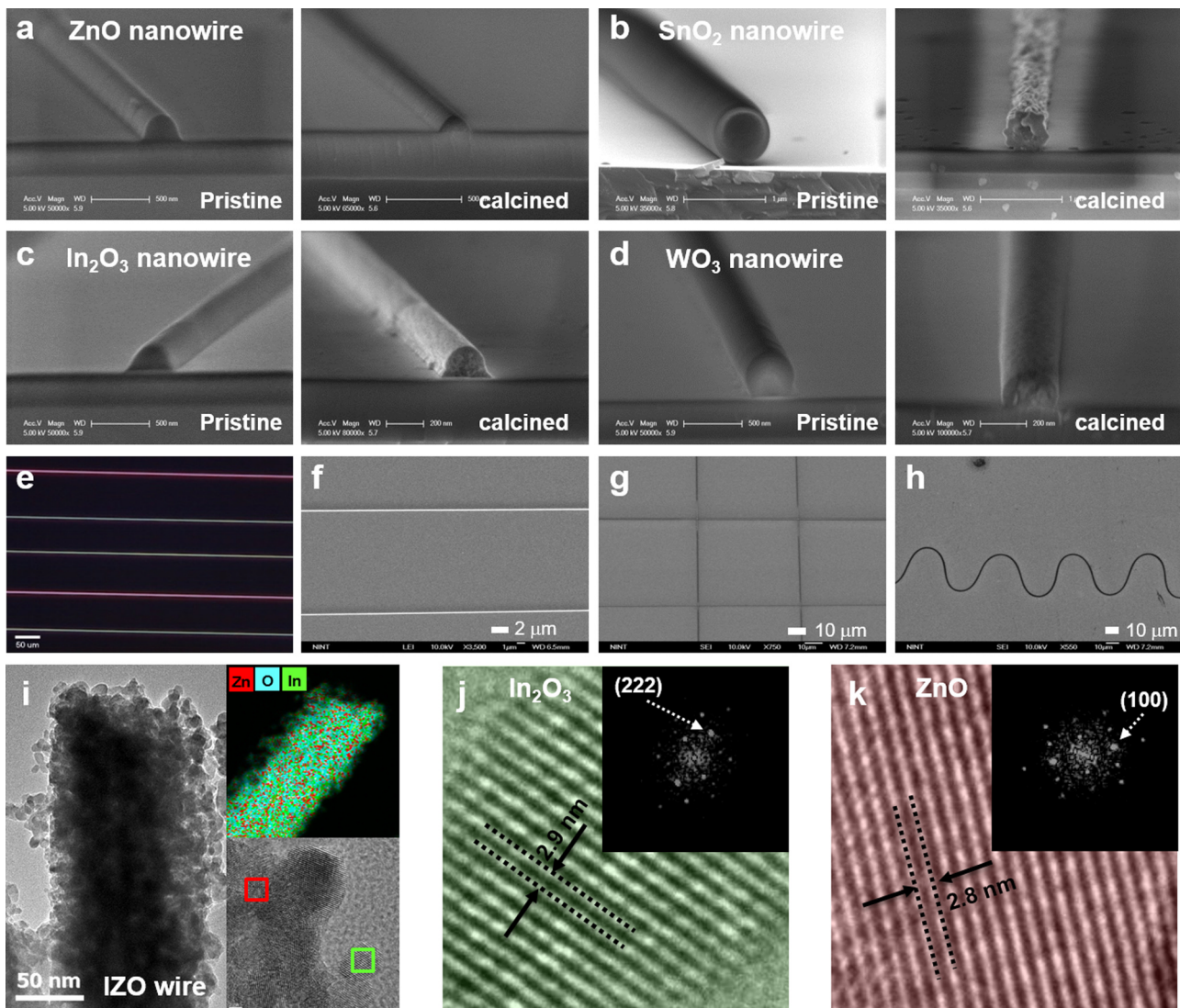


Fig. 2. SEM, OM, and HR-TEM images of various MO NWs. (a) ZnO NW, (b) SnO₂ NW, (c) In₂O₃ NW, and (d) WO₃ NW (Left: as-printed precursor/polymer wire; Right: calcined wire). (e) OM image of aligned ZnO NWs. SEM images of (f) two parallel ZnO NWs, (g) perpendicularly aligned ZnO NWs, and (h) a wavy shaped ZnO NW. (i) HR-TEM (left) and EDS mapping of IZO wire (right, up). Selected areas in (i) indicate the In₂O₃ (green) and ZnO (red) nanometer crystallites, respectively (right, down). EDS mapping of the selected regions in (i), for (j) In₂O₃ and (k) ZnO nanocrystallites at higher magnification (Insets: FFT images that provide diffraction pattern information of relevant crystal structures).

3.3. MOW field-effect transistors

To investigate the applicability of our MOWs in electronic devices, MOWFETs were fabricated. In this series of experiments, all calcination was conducted at 450 °C under O₂ ambient for 1 h. The MOWFETs of various MOWs share the same top-contact bottom-gated geometry with the channel length defined as 50 μm by a shadow mask between Au source and drain electrodes (Fig. 3a). We also quantified how the electrical characteristics and operation stability of MOWs were improved by adding MO NPs or metallic dopants such as In and Ga to the MOWs. For example, the electrical characteristics of MOW transistors using pure ZnO, ZnO with additive NPs, IZO, or indium gallium zinc oxide (IGZO) wires as active channels were compared (Fig. 3b and Fig. S8). In the following section, we discuss these strategies, which definitely increase μ and electrical stability of MOWFETs. We will also comment on the relationship between structure and electrical characteristics, which can be exploited to design and control MOWFETs.

Pure ZnO-based MOWFETs had a relatively low $\mu = 0.005 \text{ cm}^2 \text{ V}^{-1} \text{ s}^{-1}$ (Fig. S8a,b) due to the large number of grain boundaries between the nanogranular crystallites, but it was increased by two orders of

magnitude ($0.457 \text{ cm}^2 \text{ V}^{-1} \text{ s}^{-1}$) by addition of ZnO NPs (Fig. S8c,d). This increase occurs because addition of ZnO NPs improves the crystallinity and electrical conductivity of ZnO NWs (Fig. S8a-d and S9) [33]. For comparative analysis, pure ZnO and NPs-added ZnO thin films were produced from the same printing solutions of each MOW. XRD patterns showed that the pure ZnO film became crystalline with a clear (002) peak when calcined at $T_C > 450^\circ\text{C}$ (Fig. S9a), whereas $T_C = 400^\circ\text{C}$ is high enough to induce clear peak in the NP-incorporated film (Fig. S9b). At $T_C = 500^\circ\text{C}$, the NPs-doped film had sharper peaks than the pure ZnO film. This result demonstrates that the addition of NPs can improve the crystallinity of the film if other conditions that may affect the crystallinity phase (e.g., annealing condition) are fixed. X-ray photoelectron spectroscopy (XPS) was used to analyze the elemental stoichiometry and oxygen vacancies of ZnO thin films [34–36]. Various T_C were applied to relevant samples to determine the effect of additive NPs on composition changes. ZnO films and NP-added ZnO films were annealed at different T_C then their O1s core levels were compared in XPS spectra (Fig. S10a,b). Individual O1s peak were deconvoluted using a combination of Lorentzian-Gaussian functions to generate three distinct peaks. A binding-energy peak centered at

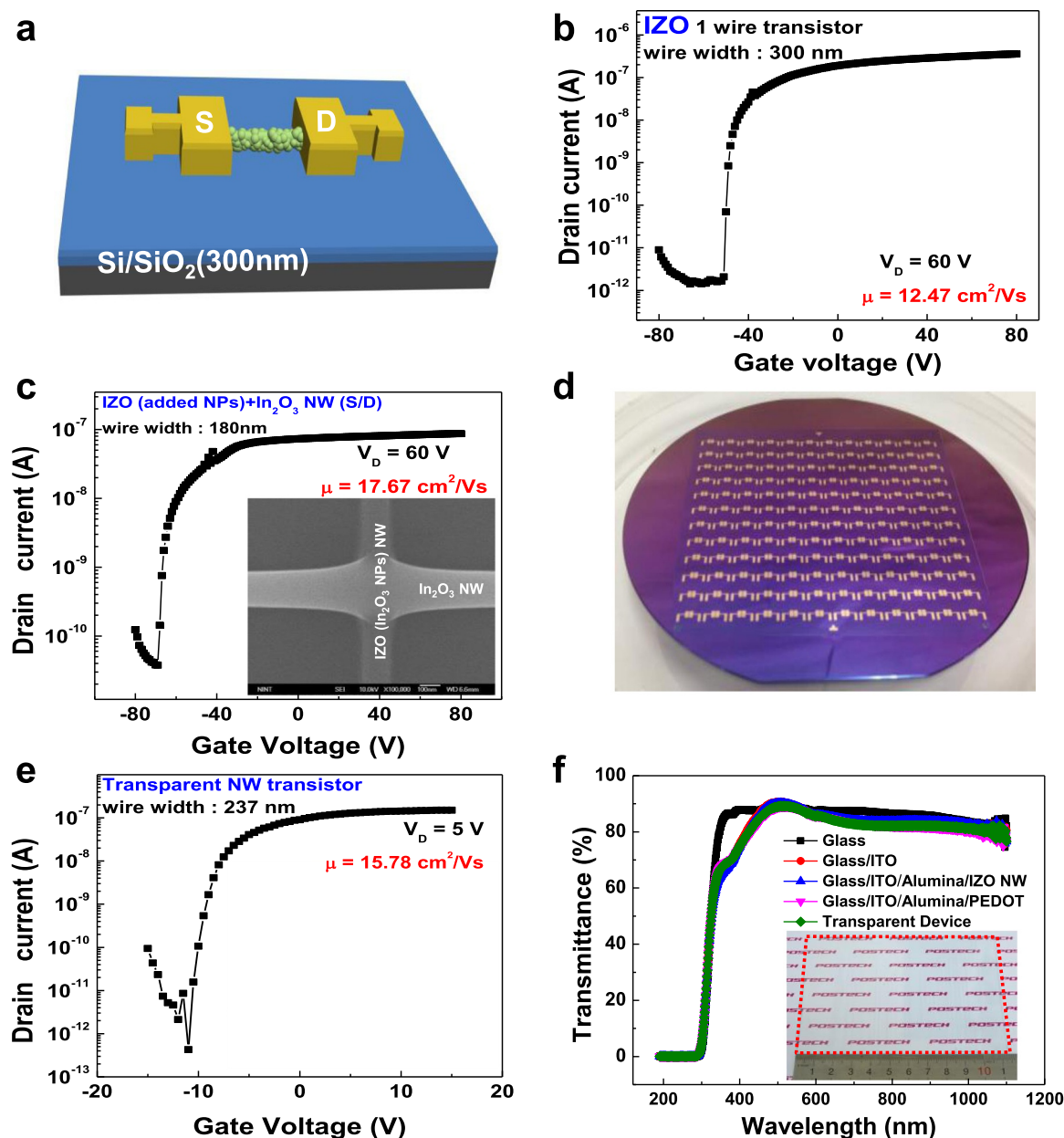


Fig. 3. (a) Schematic, images and electrical characteristics of various MOWFETs. (a) Schematic illustration of a MOWFET on 300 nm-SiO₂-covered highly doped silicon wafer as a gate insulator. (b) Transfer characteristics of an IZO NW transistor. (c) Transfer characteristics of an all-MOWFET using IZO NW (added In₂O₃ NPs) as the semiconducting channel and In₂O₃ NWs as source and drain electrodes (Inset: a SEM image of an all-MOWFET). (d) A photograph of 144 MOWFETs on a 4-in. wafer. (e) Transfer characteristics of a fully transparent MOW transistor (Inset: Schematic illustration of a transparent MOWFET on glass substrate). (f) UV-Vis spectra as a measure of transmittance of glass, glass/ITO, glass/ITO/Alumina/IZO NW, glass/ITO/Alumina/PEDOT electrodes and the finally made transparent device (Inset: a photograph of fully transparent MOW transistor arrays on glass substrate).

530.2 eV is assigned to O atoms surrounded by Zn atoms in a hexagonal wurzite structure (O_M) [34–36]. A peak centered at ~531.4 eV is assigned to O atoms in the oxygen-deficient regions (O_{VAC}) [34–36]. The peak centered at ~532.3 eV corresponds to interstitial O atoms (O_{OH}) or surface oxygen in form of -OH groups [34–36]. As T_C increases, the number of O_{OH} decreased slightly and the ratio O_M/O_{VAC} increased (Fig. S10c,d); this trend indicates a suppression of the oxygen vacancies and an increase in crystallinity (Fig. S10e,f). At all fixed calcination T_C , O_M/O_{VAC} was higher in all calcined NPs-added ZnO films than in ZnO films, e.g., at 450 °C, O_M/O_{VAC} ratio was 1.15 in NPs-added ZnO and 1.07 in ZnO films [35,36]. Crystallinity of the MO film increased as O_M/O_{VAC} increased, so addition of ZnO NPs improved crystallinity and consequently increased μ . This observation is consistent with the

crystallinity and electrical properties of the ZnO and NPs-added ZnO wires.

Another way to increase μ and electrical stability of MOWFETs is to add other metallic elements to form alloy MO. Alloy ZnO wires, such as IZO and IGZO wires, which have good μ and electrical stability, were evaluated in a transistor structure. Addition of In increased the field-effect μ (Fig. 3b) by > 20 times from 0.457 cm² V⁻¹ s⁻¹ (ZnO NPs-added ZnO wire) to 12.47 cm² V⁻¹ s⁻¹ (IZO wire), and by > 2000 times in comparison with the pure ZnO wire FET (Fig. S8a-d). Further addition of In₂O₃ NPs into IZO wires induces high crystallinity at relatively low T_C (Fig. S11).

The MOWFET transfer characteristics were analyzed by varying solution compositions of precursors (In, Zn and Ga), solution

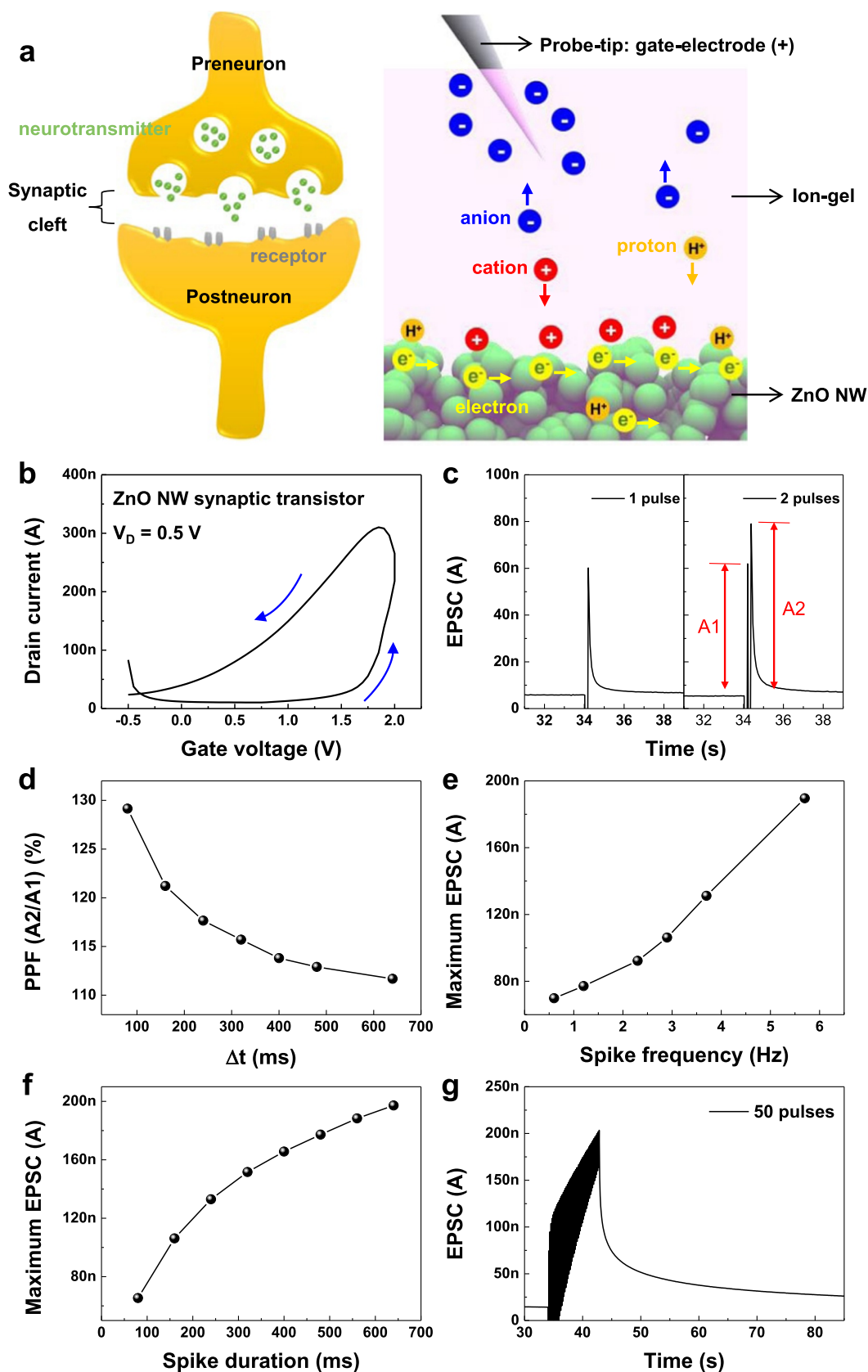


Fig. 4. Schematic and electrical responses of ZnO wire-based artificial synaptic transistor. (a) Schematic illustration and (b) transfer characteristics of highly-aligned ZnO NW synaptic transistor. (c) Excitatory postsynaptic current (EPSC) characteristics of ZnO NW synaptic transistor with single and double positive gate voltage spikes ($V_G = 2$ V, $V_D = 0.5$ V). (d) Paired-pulse facilitation (A_2/A_1) of ZnO NW synaptic transistor with different spike-to-spike intervals (Δt). Maximum EPSC of ZnO NW synaptic transistor according to (e) spike frequency and (f) spike durations. (g) EPSC of ZnO NW synaptic transistor with consecutive 50 spikes.

concentrations of a sacrificial polymer (PVAc or PVP), and T_C . The effect of In/Zn molar ratio affected the electrical properties of the IZO wire transistors (Fig. S12). As In inclusion ratio increased, the 'on' current increased and the threshold voltages V_{th} shifted negatively (Fig. S12a). These changes can be attributed to increased charge-carrier concentrations as the In fraction increases. The average field-effect μ was increased by > 2000 times as the fraction of In in IZO-microwire-based transistors increased (Fig. S12b); a similar trend was also observed in the IZO-NW-based transistor (Fig. S12c). Because the conduction band in the amorphous oxide semiconductor is composed of the unoccupied s-orbitals of a metal cation, In with large s-orbital overlap would allow for high electron μ [37]. As a result, the numbers of oxygen vacancies and interstitials are greatly increased and act as donors. Therefore, both 'on' current and field-effect μ strongly increased as In molar ratio increased (Fig. S12b,c). Additionally, excess In atoms aggregate more readily than they link to other atoms in the IZO structure, and thereby increase the number of conducting pathways for electrons and ultimately increase μ [38].

In contrast, addition of Ga suppressed both the 'on' current and the 'off' current, because Ga bonds more strongly with O than with Zn and In ions. Therefore, the presence of Ga ions decreased the generation of carriers by reducing the formation of oxygen vacancies [38–40]. Oxygen vacancies act not only as charge-carrier suppliers that contributed to current flow, but also as electron trap sites to induce instability of electrical characteristics. Therefore, addition of Ga ions strongly increased the electrical stability of the IZO. Electrical stability of IGZO wire transistors with various Ga fractions were evaluated by applying a continuous gate bias stress of $V_g = 40$ V for 10000 s (Fig. S13). The V_{th} shift and on-current variation stabilized after 6000 s in the IGZO (Ga fraction 20%) NW transistor, and became negligible after that time. The significantly improved stability of the IGZO wire transistor under bias stress may be due to reduction in the number of trap sites. Although addition of Ga reduces the 'on' current and μ of IZO, addition of Ga is an effective way to stabilize IZO's electrical properties; this stability is critical in practical applications. XRD patterns of the solution processed IGZO wire revealed an amorphous phase at various T_C (Fig. S13f), as reported previously [38].

To realize future electronic textile and transparent nanoelectronics, development of all-MOWFETs may be an essential step. All-MOWFETs were fabricated using IZO NW with added In_2O_3 NPs as the semiconducting channel, and In_2O_3 NWs as source/drain electrodes (Fig. 3c). IZO NWs (with added In_2O_3 NPs) and In_2O_3 NWs had widths of 180 nm and 185 nm (Fig. 3c, inset), respectively. Channel length (82 μm) is defined by the distance between In_2O_3 NWs. A high field-effect $\mu = 17.67 \text{ cm}^2 \text{ V}^{-1} \text{ s}^{-1}$ was obtained in this device; the improvement may be due to the compositional homogeneity between the semiconductor (IZO) and electrodes (In_2O_3). The use of MO electrodes reduces contact resistance, because they have a lower energy barrier than do metal electrodes, and therefore increase charge carrier flow at the interfaces between the active channel and the electrodes [41]. To demonstrate the feasibility of scalable production of MOWs, arrays of 144 MOWFETs were fabricated on a 4-in. wafer (Fig. 3d).

Good transmittance of visible light is one of the most important properties of MOWs; consequently they are suitable for use in transparent electronics. For demonstration, we fabricated MOW-based transparent transistor arrays using ITO-coated glass as a substrate, 30-nm-thick alumina (Al_2O_3) as gate insulator, IZO NWs as a semiconducting channel, and a conducting polymer (perfluorinated ionomer-doped poly(ethylenedioxythiophene):poly(styrene sulfonate)) (PEDOT:PSS:PFI) as transparent source and drain electrodes (Fig. 3e). Conductive lines of transparent PEDOT:PSS:PFI were also drawn using our e-NW printer; this tactic avoids the use of non-transparent metal (e.g., Ag, Au) electrodes. These transistors had reasonable electrical characteristics (Fig. 3e). Laying additional layers on glass caused no obvious decrease in its transparency (Fig. 3f and Fig. S14).

3.4. ZnO NW-based artificial synapses

Neuromorphic electronics has been emerging as a promising alternative to the conventional von Neumann computing system by mimicking massively-parallel connections and synaptic memory functions of biological neurons and synapses of a brain [42–45]. MO based-artificial synapses are highlighted as viable units rendering neuromorphic devices based on simple structures and low power consumptions [44]. Three-terminal geometric electrolyte-gated MO transistors have emulated diverse synaptic responses including short-term and long-term plasticity, thereby showed promising features for brain-inspired electronics [45,46]. In addition, solution-processed nanoscale synaptic transistor array would facilitate low-cost fabrication and high-density device integration [42]. Artificial synaptic transistors that generated biomimetic synaptic memory responses were fabricated using a ZnO NW array as an active material (Fig. 4). Ion-gel dielectric ([EMIM] [TFSI] and PS-PMMA-PS) was used to emulate a biological synaptic cleft that transmits neurotransmitters between neurons according to presynaptic action potentials (Fig. 4a). The anions in the ion gel are driven to the surface of the semiconductor by a presynaptic positive voltage spike applied to the gate electrode, and form a temporary electric double layer (EDL) at the interface between the ion gel and the semiconductors (Fig. 4a). Consecutively applied presynaptic voltage spikes separated by short time intervals (Δt) gradually increase the number of anions accumulated at the EDL; as a result the density of carriers in the semiconductor gradually increase, and generate potentiated (i.e., amplified) postsynaptic current responses. After gate voltage spikes are discontinued, the accumulated anions diffuse back into the ion-gel medium and form an equilibrium state, so the postsynaptic current rapidly decay to the original baseline [45,47]. In contrast, an ion gel doped with a small amount of moisture can not only form additional an EDL with protons (H^+) and hydroxyl (OH^-) groups but also chemisorb the protons to the MO surface [46,48]. This hydrogenation reaction can induce nonvolatile memory properties of MO channels [46,48]. Because our ZnO NW is polycrystalline, it has both Zn- and O-terminated faces. A positive gate voltage causes the protons moving to the ZnO semiconductor surface, and protons can be adsorbed on the O-terminated surface (Fig. 4a) [48]. We exposed the device to air to dope the ion gel with a small amount of moisture. In transfer characteristics, the device showed a large counterclockwise hysteresis (Fig. 4b), similar to the previously-reported ZnO device that had a moisture-doped ion gel [48].

An excitatory postsynaptic current (EPSC) characteristic of a ZnO NW-based artificial synapse device was measured with a gate voltage spike = 2 V and drain voltage = 0.5 V (Fig. 4c). After two consecutive spikes separated by short Δt , second EPSC was stronger than the first EPSC (Fig. 4c), because the second spike drove additional ions to the ZnO NW before the ions accumulated during the first spike began to diffuse back into the gel. As Δt was decreased from 640 to 80 ms, the back diffusion of the ions accumulated by the first spike became increasingly incomplete, so it yielded an increase in the EPSC induced by the second spike (Fig. 4d). This paired-pulse facilitation (PPF) response is related to short-term synaptic plasticity (i.e., memory), and its presence indicates that our ZnO NW-based artificial synaptic transistors can be used as synaptic memory for simple learning and information processing. Similarly, the maximum EPSC increased as the frequency of the spike increased (Fig. 4e). As the duration of a single spike was increased, the maximum EPSC increased because the accumulation of anions on the semiconductor surface increased (Fig. 4f). EPSC was discretely increased by a large number of repeated spikes (50 times) (Fig. 4g). After spikes, EPSC rapidly decreased, but remained higher than the original EPSC for a few tens of seconds (Fig. 4g). This effect may occur because the cations that formed the EDL rapidly diffuse back into the gel after the spikes cease, whereas the chemically-adsorbed protons on the MO surface escape slowly. These results are similar to the doping effect of organic semiconductors with an ion-gel dielectric,

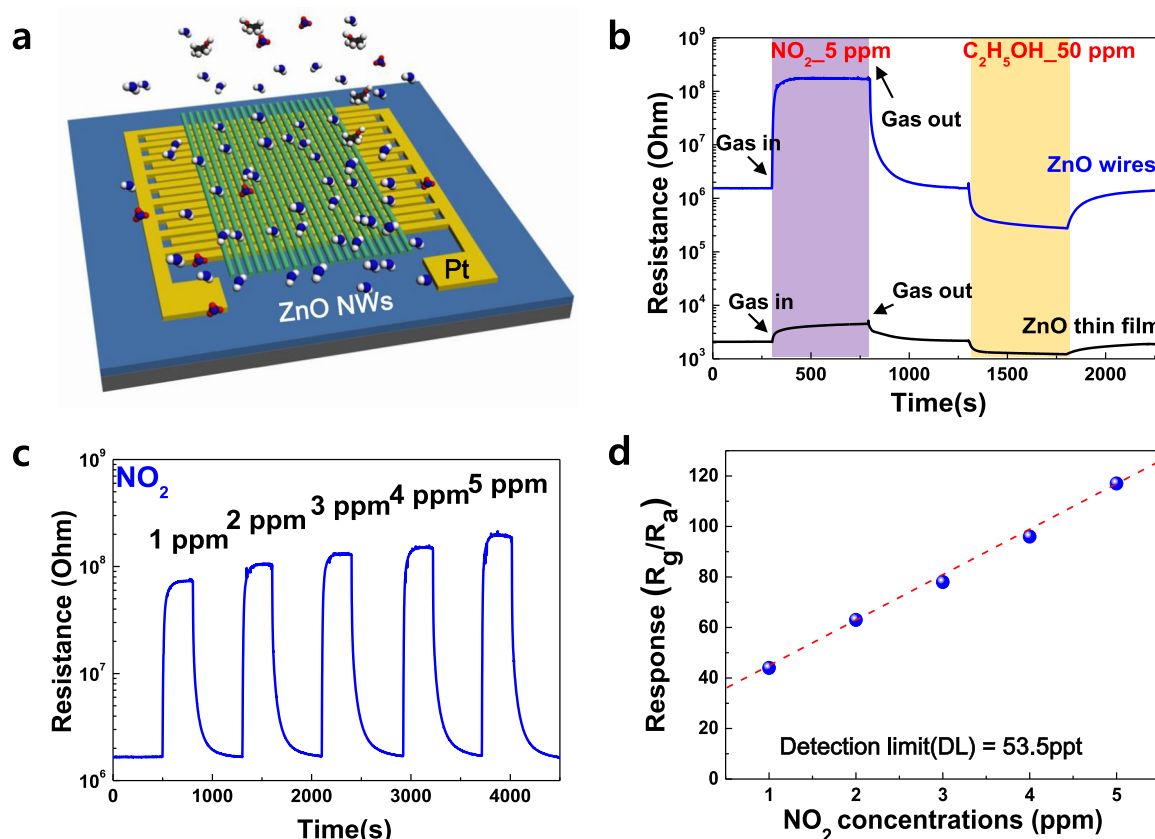


Fig. 5. Schematic and electrical responses of a ZnO wire-based gas sensor. (a) Schematic illustration of highly-aligned ZnO wires gas sensor. (b) Resistance change of the ZnO wire sensor and sputtered-ZnO thin film sensor in response to NO₂ and C₂H₅OH. (c) Response of the ZnO wire sensor to NO₂ at different concentrations ranging from 1 ppm to 5 ppm. (d) Linear fit of the responses as a function of NO₂ concentration.

which resulted in long-term plasticity in the device's response [42,43], although ZnO is ion-impermeable semiconductor [49]. Also, the synaptic responses e.g., short-term and long-term plasticity would be improved by using a proton-based electrolyte based on easy migration and chemical adsorption of protons on ZnO NW surface.

3.5. ZnO NW-based gas sensors

Chemoresistive gas sensors based on semiconducting MO nanostructures have the advantages of high sensitivity, low cost, and small size [50,51]. Among various nanostructures, 1D NWs have been regarded as promising candidates due to their large surface-to-volume ratio, which enhances the utility factor of the sensor [52–55]. The utility factor, one of the three basic factors (utility factor, transducer function, and receptor function) affecting sensing properties, is related to the ability of diffusing gas molecules to active areas of the sensors [54,55]. The wired structure maximizes the utility factor resulting in high sensing characteristics. In addition, surface space charge layers formed on the surface of individual nanograins in 1D ZnO NWs induce gas-dependent barriers for conduction electrons to across the grain boundaries, leading to effective transduction of the surface adsorption of gas molecules into an electrical resistance change of the sensor (transducer function) [54]. To see the effects of nanowire structure on sensing properties, we prepared ZnO wire and thin film gas sensors with the same thickness (~400 nm) by using the same precursor solution (Fig. 5), and measured gas responses to nitrogen dioxide (NO₂) and ethanol (C₂H₅OH) in ambient atmosphere. For n-type semiconducting MOs, negative-charged oxygen species are adsorbed on the surface of MOs under ambient air. The pre-adsorbed oxygen species on the surface

possess and trap electrons at the surface. After exposure to a reducing gas such as CO, the reducing gas is oxidized by the ionosorbed oxygen, O⁻. In the case of CO, it becomes CO₂. According to the reactions, reducing gases decrease the surface oxygen concentration and donate electrons back into the MO; as a result its resistance decreases. Opposite reactions are observed with oxidizing gases such as NO₂ [56,57]. Dynamic sensing transients of ZnO wires and thin film sensors to NO₂ and C₂H₅OH were measured (Fig. 5b). The responses were defined here as R_g/R_a for the oxidizing gas (NO₂) and R_a/R_g for the reducing gas (C₂H₅OH) where R_a is the resistance of the sensor in dry air, and R_g is the resistance of the sensor after exposure to the test gas. The ZnO wire sensor exhibited a high response of 79.5 ± 39.4 (maximum response = 143.9) to NO₂, whereas the response of a ZnO thin film was as low as 2. The ZnO wires responded much faster (67 s) than did ZnO thin films (287 s). Also, the ZnO wire sensor recovered rapidly (~90 s) (Table S1). These sensitive gas-sensing properties of the ZnO wire sensor are attributed to the longitudinal nanostructured domain structure of MOs, which probably ensures very large surface-to-volume ratio, which in turn facilitates fast mass transfer of gas molecules to and from the interaction regions, and significantly increases surface interactions between adsorbed molecules and MOs. To evaluate the detection limit of the ZnO wire sensor to NO₂, we measured the responses of the sensor to 1–5 ppm NO₂ (Fig. 5c). The responses of the ZnO sensor were 44, 63, 78, 96, and 117–1, 2, 3, 4, and 5 ppm NO₂, respectively. Although the experimentally examined lowest NO₂ concentration was 1 ppm in the present study, the theoretical detection limit was calculated to be approximately 53.5 ppt (Fig. 5d) [58]. These results suggest that our ZnO wires with high surface-to-volume ratio and porous nanostructures provide a good opportunity to increase the response of gas sensors.

4. Conclusion

We have reported a large-scale direct-printed nanoscale metal-oxide-wire (MOW) electronics with highly-aligned and arbitrarily-long MOW arrays with individually controlled positioning and alignment on the large area. The presented nanoscale MOW printing strategy shows that highly-controlled MOWs hold a significant promise in universal state-of-the art electronics. The printing process is simple, rapid, inexpensive, digitally-controlled and scalable, and is applicable to fabrication of a broad classes of pristine or doped MOWs and MOW alloys. To prove the feasibility of our approach, we demonstrated various nanoscale MOW applications. The fully-transparent all-MOW field-effect transistors (FETs) showed a high carrier mobility $\mu = 17.67 \text{ cm}^2 \text{ V}^{-1} \text{ s}^{-1}$ with high transmittance, and are therefore promising for use in transparent devices. MOW synaptic transistors showed potential applicability as nanoscale neuromorphic memory that mimics biological synaptic responses. MOW gas sensors had high response to NO_2 gas, so feasible for use in sensitive chemical and biological sensors. Our results demonstrate the technical validity and potential of our direct-printed MOW arrays in fabricating future large-scale highly-integrated nanoscale MOW electronics and provide critical insight and avenue for the viable development of large-scale MOW electronics for future needs in consumer electronics industries.

Acknowledgements

This work was supported by the Center for Advanced Soft-Electronics funded by the Ministry of Science, ICT and Future Planning as Global Frontier Project (2013M3A6A5073175). This work was also supported by Creative-Pioneering Researchers Program through Seoul National University (SNU) and the National Research Foundation of Korea (NRF) grant funded by the Korea government (Ministry of Science, ICT & Future Planning) (NRF-2016R1A3B1908431).

Appendix A. Supplementary material

Supplementary data associated with this article can be found in the online version at doi:10.1016/j.nanoen.2019.01.052.

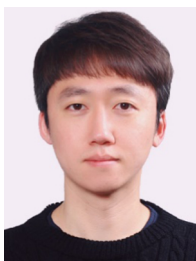
References

- [1] Y.-H. Kim, J.-S. Heo, T.-H. Kim, S. Park, M.-H. Yoon, J. Kim, M.S. Oh, G.-R. Yi, Y.-Y. Noh, S.K. Park, *Nature* 489 (2012) 128–132.
- [2] M.G. Kim, M.G. Kanatzidis, A. Facchetti, T.J. Marks, *Nat. Mater.* 10 (2011) 382–388.
- [3] J. Meyer, S. Hamwi, M. Kröger, W. Kowalsky, T. Riedl, A. Kahn, *Adv. Mater.* 24 (2012) 5408–5427.
- [4] H.T. Ng, J. Han, T. Yamada, P. Nguyen, Y.P. Chen, M. Meyyappan, *Nano Lett.* 4 (2004) 1247–1252.
- [5] S. Ju, A. Facchetti, Y. Xuan, J. Liu, F. Ishikawa, P. Ye, C. Zhou, T.J. Marks, D.B. Janes, *Nat. Nanotechnol.* 2 (2007) 378–384.
- [6] J.-M. Yun, J.-S. Yeo, J. Kim, H.-G. Jeong, D.-Y. Kim, Y.-J. Noh, S.-S. Kim, B.-C. Ku, S.-I. Na, *Adv. Mater.* 42 (2011) 4923–4928.
- [7] T. Hoare, B.P. Timko, J. Santamaria, G.F. Goya, S. Iruata, S. Lau, C.F. Stefanescu, D. Lin, R. Langer, D.S. Kohane, *Nano Lett.* 11 (2011) 1395–1400.
- [8] S.J. Kim, S.J. Choi, J.S. Jang, N.H. Kim, M. Hakim, H. Tuller, I.-D. Kim, *ACS Nano* 10 (2016) 5891–5899.
- [9] O. Lupan, V. Postica, N. Wolff, O. Polonsky, V. Duppel, V. Kaidas, E. Lazari, N. Ababii, F. Faupel, L. Kienle, R. Adelung, *Small* 13 (2017) 1602868.
- [10] J.H. Song, Y.-T. Kim, S. Cho, W.-J. Song, S. Moon, C.-G. Park, S. Park, J.M. Myoung, U. Jeong, *Adv. Mater.* 29 (2017) 1702625.
- [11] K.-M. Chiang, Z.-Y. Huang, W.-L. Tsai, H.-W. Lin, *Org. Electron.* 43 (2017) 15–20.
- [12] Y. Dong, C. Bao, W.S. Kim, *Joule* 2 (2018) 579–582.
- [13] E.B. Secor, B.Y. Ahn, T.Z. Gao, J.A. Lewis, M.C. Hersam, *Adv. Mater.* 27 (2015) 6683–6688.
- [14] J.K. Hwang, S. Cho, J.M. Dang, E.B. Kwak, K. Song, J. Moon, M.M. Sung, *Nat. Nanotechnol.* 5 (2010) 742–748.
- [15] M.S. Onses, C. Song, L. Williamson, E. Soutanto, P.M. Ferreira, A.G. Alleyne, P.F. Nealey, H. Ahn, J.A. Rogers, *Nat. Nanotechnol.* 8 (2013) 667–675.
- [16] W.-T. Park, Y.-Y. Noh, J. Mater. Chem. C. 5 (2017) 6467–6470.
- [17] G. Xue, J. Wu, C. Fan, S. Liu, Z. Huang, Y. Liu, B. Shan, H.L. Xin, Q. Miao, H. Chena,

- Hanyang Li, *Mater. Horiz.* 3 (2016) 119–123.
- [18] G. Giri, E. Verploegen, S.C.B. Mannsfeld, S. Atahan-Evrenk, D.H. Kim, S.Y. Lee, H.A. Becerril, A. Aspuru-Guzik, M.F. Toney, Z. Bao, *Nature* 480 (2011) 504–508.
- [19] S.-Y. Min, T.-S. Kim, B.J. Kim, H. Cho, Y.-Y. Noh, H. Yang, J.H. Cho, T.-W. Lee, *Nat. Commun.* 4 (2013) 1773.
- [20] Y. Lee, T.-S. Kim, S.-Y. Min, W. Xu, S.-H. Jeong, H.-K. Seo, T.-W. Lee, *Adv. Mater.* 26 (2014) 8010–8016.
- [21] Y. Lee, S.-Y. Min, T.-W. Lee, *Macromol. Mater. Eng.* 302 (2017) 1600507.
- [22] S.-Y. Min, T.-S. Kim, Y. Lee, H. Cho, W. Xu, T.-W. Lee, *Small* 11 (2015) 45–62.
- [23] Y. Lee, S.-Y. Min, T.-S. Kim, S.-H. Jeong, J.Y. Won, H. Kim, W. Xu, J.K. Jeong, T.-W. Lee, *Adv. Mater.* 28 (2016) 9109–9116.
- [24] S. Lee, J. Kim, J. Choi, H. Park, J. Ha, Y. Kim, J.A. Rogers, U. Paik, *Appl. Phys. Lett.* 100 (2012) 102108.
- [25] Y.G. Lee, W.-S. Choi, *ACS Appl. Mater. Interfaces* 6 (2014) 11167–11172.
- [26] S. Jeong, J.-Y. Lee, S.S. Lee, Y.-H. Seo, S.-Y. Kim, J.-U. Park, B.-H. Ryu, W. Yang, J. Moon, Y. Choi, *J. Mater. Chem. C* 1 (2013) 4236–4243.
- [27] H. Wu, D. Lin, R. Zhang, W. Pan, *J. Am. Ceram. Soc.* 91 (2008) 656–659.
- [28] X. Zou, X. Liu, C. Wang, Y. Jiang, Y. Wang, X. Xiao, J.C. Ho, J. Li, C. Jiang, Q. Xiong, L. Liao, *ACS Nano* 7 (2013) 804–810.
- [29] A.K. Nayak, R. Ghosh, S. Santra, P.K. Guha, D. Pradhan, *Nanoscale* 7 (2015) 12460–12473.
- [30] J. Liu, G. Chen, Y. Yu, Y. Wu, M. Zhou, H. Zhang, C. Lv, Y. Zheng, F. He, *RSC Adv.* 5 (2015) 44306–44312.
- [31] J. Gim, V. Mathew, J. Lim, J. Song, S. Baek, J. Kang, D. Ahn, S.-J. Song, H. Yoon, *J. Mater. Sci. Rep.* 2 (2012) 946.
- [32] F.P. Incropera, D.P. Dewitt, T.L. Bergman, A.S. Lavine, *Fundamentals of Heat and Mass Transfer*, 6th edn, John Wiley & Sons, 2007.
- [33] S.Y. Cho, Y.H. Kang, J.-Y. Jung, S.Y. Nam, J. Lim, S.C. Yoon, D.H. Choi, C. Lee, *Chem. Mater.* 24 (2012) 3517–3524.
- [34] Y. Fang, Y. Wang, L. Gu, R. Lu, J. Sha, *Opt. Express* 21 (2013) 3492–3500.
- [35] K. Hong, S.H. Kim, K.H. Lee, C.D. Frisbie, *Adv. Mater.* 25 (2013) 3413–3418.
- [36] H. Bong, W.H. Lee, D.Y. Lee, B.J. Kim, J.H. Cho, K. Cho, *Appl. Phys. Lett.* 96 (2010) 192115.
- [37] C.Y. Koo, K. Song, T. Jun, D. Kim, Y. Jeong, S.-H. Kim, J. Ha, J. Moon, *J. Electrochem. Soc.* 157 (2010) J111–J115.
- [38] G.H. Kim, B.D. Ahn, H.S. Shin, W.H. Jeong, H.J. Kim, H.J. Kim, *Appl. Phys. Lett.* 94 (2009) 233501.
- [39] D. Kim, C.Y. Koo, K. Song, Y. Jeong, J. Moon, *Appl. Phys. Lett.* 95 (2009) 103501.
- [40] J.H. Lim, J.H. Shim, J.H. Choi, J. Joo, K. Park, H. Jeon, M.R. Moon, D. Jung, H. Kim, H.-J. Lee, *Appl. Phys. Lett.* 95 (2009) 012108.
- [41] S. Lee, H. Park, D.C. Paine, *J. Appl. Phys.* 109 (2011) 063702.
- [42] W. Xu, S.-Y. Min, H. Hwang, T.-W. Lee, *Sci. Adv.* 2 (2016) e1501326.
- [43] Y. Kim, A. Chortos, W. Xu, Y. Liu, J.Y. Oh, D. Son, J. Kang, A.M. Foudeh, C. Zhu, Y. Lee, S. Niu, J. Liu, R. Pfattner, Z. Bao, T.-W. Lee, *Science* 360 (2018) 998–1003.
- [44] S. Park, J. Noh, M.-L. Choo, A.M. Sheri, M. Chang, Y.-B. Kim, C.J. Kim, M. Jeon, B.-G. Lee, B.H. Lee, H. Hwang, *Nanotechnology* 24 (2013) 384009.
- [45] X. Wan, P. Feng, G.D. Wu, Y. Shi, Q. Wan, *IEEE Electron Device Lett.* 36 (2015) 204–206.
- [46] J. Zhou, Y. Liu, Y. Shi, Q. Wan, *IEEE Electron Device Lett.* 35 (2014) 280–282.
- [47] H. Yuan, H. Shimotani, A. Tsukazaki, A. Ohtomo, M. Kawasaki, Y. Iwasa, *Adv. Funct. Mater.* 19 (2009) 1046–1053.
- [48] H. Yuan, H. Shimotani, A. Tsukazaki, A. Ohtomo, M. Kawasaki, Y. Iwasa, *J. Am. Chem. Soc.* 132 (2010) 6672–6678.
- [49] K. Hong, Y.H. Kim, S.H. Kim, W. Xie, W.D. Xu, C.H. Kim, C.D. Frisbie, *Adv. Mater.* 26 (2014) 7032–7037.
- [50] S. Capone, A. Forleo, L. Francioso, R. Rella, P. Siciliano, J. Spadavecchia, D.S. Presicce, A.M. Taurino, *J. Optoelect. Adv. Mater.* 5 (2003) 1335–1348.
- [51] N. Yamazoe, K. Shimano, *Sens. Actuators B: Chem.* 138 (2009) 100–107.
- [52] A. Kolmakov, D. Klenov, Y. Lilach, S. Stemmer, M. Moskovits, *Nano Lett.* 5 (2005) 667–673.
- [53] F. Favier, E.C. Walter, M.P. Zach, T. Benter, R.M. Penner, *Science* 293 (2001) 2227–2231.
- [54] N. Yamazoe, K. Shimano, *J. Sens.* 2009 (2009) 875704.
- [55] E. Comini, G. Faglia, G. Sberveglieri, Z. Pan, Z.L. Wang, *Appl. Phys. Lett.* 81 (2002) 1869–1871.
- [56] K.D. Schierbaum, U. Weimar, W. Göpel, R. Kowalkowski, *Sens. Actuators B: Chem.* 3 (1991) 205–214.
- [57] A. Kolmakov, Y. Zhang, G. Cheng, M. Moskovits, *Adv. Mater.* 15 (2003) 997–1000.
- [58] J. Li, Y. Lu, Q. Ye, M. Cinke, J. Han, M. Meyyappan, *Nano Lett.* 3 (2003) 929–933.



Tae-Sik Kim received her Ph.D. (2016) in Materials Science and Engineering from Pohang University of Science and Technology (POSTECH), Korea. She is currently working in Samsung Display, Korea as a professional researcher. Her research focuses on controllable organic and inorganic nanowires for nano-electronic applications.



Yeongjun Lee is a postdoctoral researcher in Materials Science and Engineering at Seoul National University, Korea. He received his M.S. (2014) and Ph.D. (2018) in Materials Science and Engineering from Pohang University of Science and Technology (POSTECH), Korea. His research interests include printed electronics, nanowire electronics, stretchable polymer electronics, and organic neuromorphic electronics.



Sung-Yong Min received his Ph.D. (2015) in Materials Science and Engineering from Pohang University of Science and Technology (POSTECH), Korea. He is currently working in LG Chem R&D Campus Daejeon, Korea as a professional researcher. His research focuses on controllable metallic wire printing for all-wire electronics.



Wentao Xu is a professor at Nankai University, China. He received his B.S. from Beijing Normal University, and Ph.D. in Chemical Engineering from Pohang University of Science and Technology (POSTECH) in February 2012. He worked as a research associate professor at POSTECH and Seoul National University. His research interests include synapse-emulating electronic devices, nonvolatile memory devices, graphene electronics, and organic field-effect transistors.



Tae Hoon Kim is studying for his Ph.D course in the Department of Materials Science and Engineering of Seoul National University. His research interests include the fabrication of chemoresistive sensors based on metal oxides and two-dimensional materials and the demonstration of electronic nose.



Yeon Hoo Kim received his Ph.D degree from the Department of Materials Science and Engineering of Seoul National University in 2018. Now he is a postdoctoral research associate in Los Alamos National Laboratory. His research interests include the synthesis and in-situ analysis of two-dimensional materials and their applications.



Ho Won Jang joined the Department of Materials Science and Engineering of Seoul National University in 2012 and is currently an associate professor. He received his Ph.D from the Department of Materials Science and Engineering of POSTECH in 2004. He worked in University of Wisconsin-Madison as a research associate and Korea Institute of Science and Technology as a senior research scientist. His research interests are the synthesis of nanostructured oxide thin films, two-dimensional materials, and halide perovskites and their applications to various devices including chemical sensors, solar water splitting cells, photovoltaics, and memristors.



Miseong Kim received her M.S. (2013) in Materials Science and Engineering from Pohang University of Science and Technology (POSTECH), Korea. She is currently working in LG Display, Korea. Her research focuses on controllable organic and inorganic hybrid nanowires for nano-electronic applications.



Tae-Woo Lee is an associate professor in Materials Science and Engineering at Seoul National University, Korea. He received his Ph.D in Chemical Engineering from KAIST, Korea in 2002. He joined Bell Laboratories, USA as a postdoctoral researcher and worked in Samsung Advanced Institute of Technology as a member of the research staff (2003–2008). He was an associate professor in Materials Science and Engineering at Pohang University of Science and Technology (POSTECH), Korea until Aug, 2016. His research focuses on printed flexible electronics based on organic and organic-inorganic hybrid materials for flexible displays, solid-state lightings, and solar-energy-conversion devices.